Quantum charge and spin pumping in monolayer phosphorene

Hossein Nikoofard [1,2] Mahdi Esmaeilzadeh [1,*] Ebrahim Heidari-Semiromi,[2] and Jia Tao Sun [3]

[1]*Department of Physics, Iran University of Science and Technology, Tehran 16844, Iran*
[2]*Department of Physics, University of Kashan, Kashan 87317-53153, Iran*
[3]*Beijing National Laboratory for Condensed Matter Physics and Institute of Physics, Chinese Academy of Sciences, Beijing 100190, China*

We study quantum-charge and spin-transport properties and the effects of in-plane strain on the charge and spin currents in a phosphorene monolayer using an adiabatic pumping regime. To achieve this goal, we proposed a device with three external ac gate voltages as oscillating potential barriers that are responsible for the generation of dc pumped current. Using exchange magnetic field induced by proximity effect of a ferromagnetic insulator, we determine the conditions in which fully spin-polarized current and pure spin current (with zero charge current) can be obtained. It is shown that the pumped current in the three-barrier case is about two times greater than the pumped current in a two-barrier system. The effect of strain is investigated and it is found that the spin current increases up to two orders of magnitude by applying the uniaxial strain which shows that the proposed device has high sensitivity to strain and could be used as straintronic devices such as strain switches and strain sensors. Also, in the same conditions, the pumped current in phosphorene is two, four, and five orders of magnitude greater than the pumped current in MoS_2, silicene, and graphene, respectively. These properties show that phosphorene can be considered as a two-dimensional (2D) semiconductor with great potential for the fabrication of novel spintronic and straintronic devices that can overcome some of the limitations exhibited by conventional 2D materials.

I. INTRODUCTION

In recent decades, 2D materials have attracted great attention due to beneficial attributes and promising potential for fabrication of nanoscale electronic devices with high performance and low waste of energy. Graphene, as a first 2D material with numerous applications, due to having zero-energy band gap and a small on/off ratio, leads to limitations for tuning of spin transport in spin-based devices like spin field-effect transistors [1]. So, researchers have looked for properties of other 2D materials from the graphene family such as silicene [2], germanene, and transition-metal dichalcogenides (TMDs) [3] for use in quantum transport. MoS_2 as a famous TMD, although having an energy band gap, due to relatively low carrier mobility and large spin-orbit coupling has some restrictions for using in integrated circuits with high speed [4]. Recently, phosphorene as a monolayer of black phosphorus (BP) resolved these restrictions due to having a widely tunable band gap, weak spin-orbit coupling, high electron and hole mobilities, high conductivity, and high on/off ratio [5–8]. High anisotropy in the nature of phosphorene, due to a puckered structure, is responsible for unique electronic and optical behaviors compared to other conventional 2D materials [4,5]. Hence, this material can be a desirable candidate for electronic devices with successful operations [9] versus silicon or graphene-based devices [10,11]. Fortunately, phosphorene is synthesized experimentally through several methods, including liquid exfoliation and mechanical cleavage [12,13]. These particularities make it more favorable in thermal and

electrical transports [5,14–16] and in the field of spintronics, photovoltaics, and optoelectronics [9].

The above-mentioned significant properties of phosphorene encourage researchers to investigate the effects of strain, electric, and magnetic fields on the charge and spin transport through this material. It was shown that the conductance anisotropy of phosphorene is largely tunable by an external electric field and this field reverses the directions of minimum and maximum conductance [17]. Also, the electric field has different effects on the edge states with an even or odd number of the chain in zigzag phosphorene nanoribbons that introduce this material for fabricating of field-effect transistors [18]. The colossal modulations in the conductivity are observed in a phosphorene nanoribbon in the proximity of a benzene molecule under certain conditions of strain and doping [19]. In addition, the strong dependence of electronic conductivity of the phosphorene monolayer on strain is reported [20]. Moreover, quantum transport in phosphorene is studied through the modification of strain-induced band gap [21]. Recently, spin-dependent conductance and Hartman effect have been studied in monolayer phosphorene in the presence of an exchange field [22]. Furthermore, spin filtering can occur in phosphorene nanoribbon in the presence of a ferromagnetic strip and an external electric field [23]. Also, the design of phosphorene spin valves [24] and the fabrication of field-effect transistors based on few-layer phosphorene [12] have proved the beneficial effects of this material to be widely used in next-generation electronic devices [5–8,12].

Quantum pumping is a prospect for generation and controlling of spin and charge transport by using periodic variation of physical parameters such as ac gate potential without using an external bias [25]. In this phenomenon, electronic
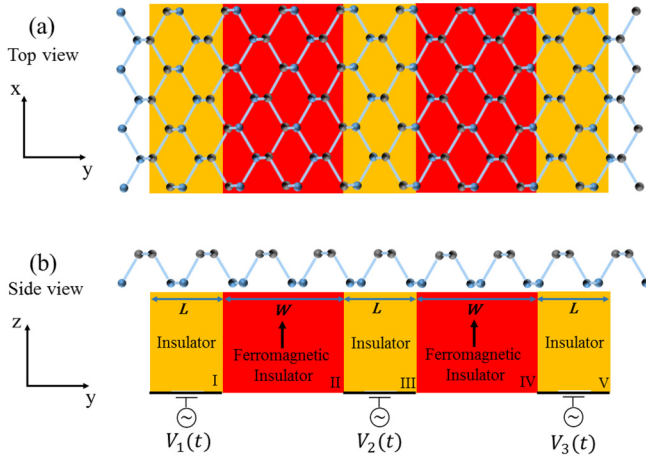
---
*mahdi@iust.ac.ir

FIG. 1. (a) Top and (b) side schematic views of a quantum charge- and spin-pumping device based on phosphorene monolayer. Three oscillating potentials $V_1(t)$, $V_2(t)$, and $V_3(t)$ are applied in regions I, III, and V to generate dc current. For excluding the permeate of gate current, we use an insulator layer shown in yellow for each gate. Also, two exchange magnetic fields with parallel or antiparallel configuration induced by proximity effect of two ferromagnetic insulators (shown in red) are applied in regions II and IV to induce spin-resolved current. The black arrows indicate the direction of exchange magnetic fields which show parallel configuration in this figure.

waves interfere with each other due to the phase difference between ac gate voltages and thus a dc current flows in the system. This method was proposed by Thouless from a theoretical approach [26] but with realization of this theory in a quantum dot [27], it has been widely investigated in nanoscale systems [28–32]. For example, the pure spin current has been theoretically studied in graphene nanoribbons in the adiabatic pumping regime [33]. When the transmission time of carriers throughout the system is much lower than the period of oscillating voltages, the adiabatic quantum pumping regime is valid. Charge pumped current is investigated in an open quantum dot [28], mesoscopic system [30,31], and in a monolayer graphene sheet in the presence of a magnetic field [34] or defects [35]. The spin and valley pumping currents can be generated in silicene and MoS_2 monolayers due to a perpendicular electric field in the presence of an exchange magnetic field [36,37]. Furthermore, spintronic devices that work based on the pumping method can have a significant effect on the data transfer speed in quantum computing and energy saving [32,36]. However, the quantum pumping transport in the phosphorene channel has received no attention.

In the present paper, quantum pumping properties are studied in a phosphorene monolayer in which three ac gate volt-

ages, as potential barriers, are applied on the system and two ferromagnetic insulators are used to induce exchange magnetic fields. We find conditions in which fully spin-polarized current and pure spin current (with zero charge current) can be obtained. It is shown that increasing the number of barriers has a significant effect to increase the magnitude of charge current in phosphorene. Also, we show that in the presence of uniaxial tensile strain (applied in the armchair direction), the pumped spin current increases up to two orders of magnitude which indicates that phosphorene is not only suitable for spintronic applications but also it is suitable for straintronic applications such as strain switches and strain sensors. A comparison between the charge pumped currents in phosphorene and the other well-known 2D materials shows that the charged pumped current in phosphorene is several orders of magnitude greater than that of graphene, silicene, and MoS_2. The results presented here will be valuable for researchers to consider phosphorene monolayer as a promising candidate for straintronics and also for producing spin transistors with a dominant performance, extremely low power consumption, and large processing speeds.

The rest of the paper is organized as follows. In Sec. II, the Hamiltonian of the system and analytical formula based on scattering matrix (S matrix) are presented for calculating charge and spin-dependent currents. In Sec. III, numerical results of charge- and spin-pumping properties of phosphorene and the influence of strain on pumped currents are presented and discussed. Finally, a summary and conclusion are given in Sec. IV.

II. MODEL AND HAMILTONIAN

We consider a quantum pumping device consisting of a phosphorene monolayer with width w as shown in Fig. 1. To pump current, three oscillating potentials are applied in regions with yellow and to generate spin-resolved current, two exchange magnetic fields induced by proximity effect of ferromagnetic insulators are used (see Fig. 1). The Hamiltonian of this system in a tight-binding model is given by [22]

$$\hat{H} = \hat{H}_0(k) \otimes \hat{\sigma}_0 - \hat{\lambda}_0 \otimes M\hat{\sigma}_z + eV\hat{\lambda}_0 \otimes \hat{\sigma}_0, \qquad (1)$$

where $\hat{\sigma}_0$ and $\hat{\lambda}_0$ are a set of Pauli matrices, M is the normalized strength of exchange magnetic fields, $-e$ is the electron charge, and V is the value of oscillating potentials. Using a two-band model for the Hamiltonian of phosphorene proposed in Ref. [38], we can write the Hamiltonian $\hat{H}_0$ in Eq. (1) at the Γ point as [38]

$$\hat{H}_0(k) = \begin{pmatrix} u_0 + \eta_x k_x^2 + \eta_y k_y^2 & \delta + \gamma_x k_x^2 + \gamma_y k_y^2 + i\chi k_y \\ \delta + \gamma_x k_x^2 + \gamma_y k_y^2 - i\chi k_y & u_0 + \eta_x k_x^2 + \eta_y k_y^2 \end{pmatrix}, \qquad (2)$$

where $u_0 = -0.42$ eV, $\eta_x = 0.58$ eVÅ^2, $\eta_y = 1.01$ eVÅ^2, $\delta = 0.76$ eV, $\chi = 5.25$ eVÅ, $\gamma_x = 3.93$ eVÅ^2, and

$\gamma_y = 3.83$ eVÅ^2, which are obtained from the hopping parameters in tight-binding calculations [38]. The effects of

applied uniaxial strain can be taken into account through the modification of hopping parameters and, as a result, modification of the above-mentioned constants [38]. The modified hopping integral t under strain effect, by using the Harrison rule, is as follows [39,40]:

$$t/t_0 \approx 1 - 2(\alpha_x \varepsilon_x + \alpha_y \varepsilon_y + \alpha_z \varepsilon_z), \quad (3)$$

where t_0 is the hopping integral, ε_i ($i = x, y, z$) are the strain components, and the coefficients of α_i are related to the geometrical parameter in undeformed phosphorene [41].

The Hamiltonian in Eq. (1) can act on wave function $\Psi_\sigma(k) = \psi(k) \otimes \xi_\sigma$, where $\psi(k)$ and ξ_σ are the eigenvectors of momentum (related to the conduction-valence band) and spin subspaces. The modulation of oscillating potentials breaks both time reversal and spatial symmetries and generates pumped current. The oscillating potentials are considered as $V_1(t) = V_{01} + \delta V_1 \sin(\omega t)$, $V_2(t) = V_{02} + \delta V_2 \sin(\omega t + \varphi)$, and $V_3(t) = V_2(t)$. Here V_{01} and V_{02} are the static part of potentials, δV_1 and δV_2 are the ac amplitude, ω is the frequency of oscillation, and φ is the phase difference between the left and central/right potentials. In the pumping device shown in Fig. 1, we have five regions I, II,...,V (including three oscillating potentials and two ferromagnetic wells). We can confine each individual region with boundaries y_{1j} and y_{2j} ($j = $ I, II,...,V) [42]. Then by using wave functions $\Psi_\sigma(k)$ in $y < y_{1j}$, $y_{1j} < y < y_{2j}$, and $y > y_{2j}$ [22] and applying the boundary conditions at y_{1j} and y_{2j} (not shown in figure), the reflection and transmission coefficients can be obtained for the incident wave from the left side of region j as follows:

$$r_j = \frac{2i(\lambda\lambda' \cos\theta_q - \lambda^2 \cos\theta_k) \sin[q_y(y_{2j} - y_{1j})] e^{2ik_y(y_{1j})} e^{-i\theta_k}}{A_1}, \quad (4)$$

$$t_j = \frac{-2\lambda\lambda'(\sin\theta_k)(\sin\theta_q) \exp[-ik_y(y_{2j} - y_{1j})]}{A_1}, \quad (5)$$

where

$$A_1 = \exp[iq_y(y_{2j} - y_{1j})][1 - \lambda\lambda' \cos(\theta_q - \theta_k)]$$
$$- \exp[-iq_y(y_{2j} - y_{1j})][1 - \lambda\lambda' \cos(\theta_q + \theta_k)], \quad (6)$$

k_y is the y component of the wave vector for incoming/outgoing waves to the region and q_y is the y component of wave vector inside the region, k_x is the x component of the wave vector that is preserved throughout the region due to invariance along this direction and $\lambda, \lambda' = 1(-1)$ is defined for electron (hole) carriers. In Eqs. (4)–(6), q_y depends on the magnetic field (M) and gate potential (V) and can be obtained by using the eigenvalues of the Hamiltonian $\hat{H}$. The eigenvalues and q_y are given by

$$E = eV - \sigma M + u_0 + \eta_x k_x^2 + \eta_y q_y^2$$
$$\pm \sqrt{\left(\delta + \gamma_x k_x^2 + \gamma_y q_y^2\right)^2 + (\chi q_y)^2} \quad (7)$$

and

$$q_y = \sqrt{\frac{-b_1 \pm \sqrt{b_1^2 - 4a_1 c_1}}{2a_1}}, \quad (8)$$

where

$$a_1 = \eta_y{}^2 - \gamma_y{}^2,$$
$$b_1 = -2(E - u_0 - eV + \sigma M - \eta_x k_x^2)\eta_y - \chi^2$$
$$\quad - 2(\delta + \gamma_x k_x^2)\gamma_y, \quad (9)$$
$$c_1 = (E - u_0 - eV + \sigma M - \eta_x k_x^2)^2 - (\delta + \gamma_x k_x^2)^2.$$

In Eqs. (4)–(6), the phase factors θ_k and θ_q, in the polar coordinates, are as follows:

$$\theta_k = \arctan\left(\frac{\chi k_y}{\delta + \gamma_x k_x{}^2 + \gamma_y k_y{}^2}\right), \quad (10)$$

$$\theta_q = \arctan\left(\frac{\chi q_y}{\delta + \gamma_x k_x{}^2 + \gamma_y q_y{}^2}\right). \quad (11)$$

The scattering matrix for each region is defined by $S_j = [(r_j, t_j)^T (t'_j, r'_j)^T]$, where the superscript T stands for transpose, r'_j and t'_j are reflection and transmission coefficients for incident electrons from the right side of the region j, respectively [42]. Using the individual S_j, the S matrix for whole system can be determined as $S = S_1 S_2, ..., S_5$. Then the pumped current can be obtained with a general formula [36,43],

$$I_k^\sigma = \frac{\omega e(\sin\varphi)\delta V_1 \delta V_2}{2\pi} \sum_{\alpha=1} \sum_{\beta=1,2} \text{Im}\left(\frac{\partial (S_{\alpha\beta}^\sigma)^*}{\partial V_1} \frac{\partial S_{\alpha\beta}^\sigma}{\partial V_2}\right), \quad (12)$$

where index α is related to outgoing modes from the left lead, β is related to incoming modes to the channel from left and right leads [44], and index σ denotes the spin direction. Considering the weak pumping regime, $V_0 \gg \delta V_0$, the derivations $\frac{\partial S^\sigma}{\partial V_i}$ become independent of time. Because of including all of the quantum states for a specific value of Fermi energy, summation over k_x is required. Using $k_x = -k \sin\phi$ and $k_y = k \cos\phi$, where ϕ is the incident angle of electron to barrier, the summation can be converted to an integral over ϕ (see Appendix A for more details) and the total pumped current can be written as

$$I^\sigma = \lim_{w \to \infty} \sum_k I_k^\sigma = \frac{w}{2\pi} \int_{-k_x^{\max}}^{+k_x^{\max}} I_k^\sigma(k_x) dk_x$$
$$= \frac{w}{2\pi} \int_{-\frac{\pi}{2}}^{\frac{\pi}{2}} I_\phi^\sigma(\phi) d\phi. \quad (13)$$

The spin current, charge current, and spin polarization can be defined by the following relations:

$$I_s = I^\uparrow - I^\downarrow, \quad (14)$$

$$I_c = I^\uparrow + I^\downarrow, \quad (15)$$

and

$$P_s = \frac{|I^\uparrow| - |I^\downarrow|}{|I^\uparrow| + |I^\downarrow|}. \quad (16)$$

Here $I^\uparrow$ and $I^\downarrow$ are spin-up and spin-down currents, respectively. The above equations show that (a) if $I^\uparrow = -I^\downarrow$, charge current is zero and pure spin current is observed, (b) if $I^\uparrow = I^\downarrow$, unpolarized current exists, and (c) if $I^\uparrow = 0$ and $I^\downarrow \neq 0$
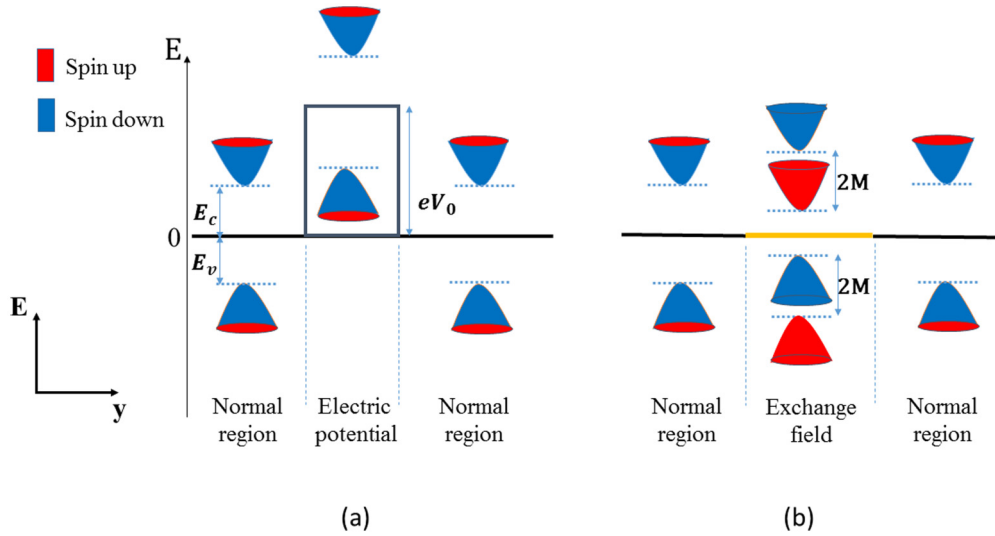
FIG. 2. Schematic view of the band structure of phosphorene monolayer when an electric potential or an exchange magnetic field is applied in central region. (a) Electric potential causes both valence and conduction bands to move as much as eV_0. (b) Exchange field breaks spin degeneracy and causes to move spin-up (-down) bands as much as $-M$ (M). The red (blue) color corresponds to the spin-up (spin-down) bands.

or $I^\downarrow = 0$ and $I^\uparrow \neq 0$, the fully spin-polarized current can be achieved.

III. RESULTS AND DISCUSSION

In this section, we present a numerical study based on equations given in Sec. II. For numerical calculation, we consider a sheet of phosphorene with width $w = 10$ μm and three oscillating potentials are applied in regions with the same length $L = 15$ nm as shown in Fig. 1. For simplicity, we consider $u_0 = 0$ and thus $E_c = 760$ meV and $E_v = -760$ meV where $E_c(E_v)$ is the value of the minimum of conduction (maximum of valence) band energy [22]. Also, two exchange magnetic fields, induced by proximity effect of two ferromagnetic insulators, are applied in regions between the oscillating barriers with the same length $W = 30$ nm (see Fig. 1). Moreover, we consider the static part of potential energies $eV_{01} = eV_{02} = eV_{03} = 1875$ meV, the ac amplitude of them $e\delta V_1 = e\delta V_2 = e\delta V_3 = 0.1$ meV, and their oscillation frequency $\omega = 5$ GHz. The phase difference between the first potential barrier and second/third ones for having maximum dc pumped current is chosen as $\varphi = \pi/2$. The normalized value of exchange magnetic field is considered as $M = 200$ meV.

To better understand the effect of external electric potential and exchange field, Fig. 2 shows a schematic view of conduction and valence bands of the phosphorene-based device under influence of electric potential and exchange field. In the presence of electric potential as shown in Fig. 2(a), the spin degeneracy remains unchanged but both bands move as much as the height of the potential barrier (i.e., eV_0). Applying exchange field, spin degeneracy breaks down which causes spin splitting as shown in Fig. 2(b). In this case, the exchange field acts as a barrier (well) for carriers with spin down (up). Also, if the direction of magnetization is reversed, the spin-up and spin-down bands act reversely.

In the absence of exchange fields ($M = 0$), the pumped spin-resolved currents $I^\uparrow$ and $I^\downarrow$ versus the Fermi energy are shown in Fig. 3. Regarding values of the band gap of phosphorene and external potentials, we consider an allowable range of Fermi energy (i.e., $E > 800$ meV) for incident electrons to flow throughout the system. It is observed that spin-up and spin-down currents are completely coincident for all values of the Fermi energy because the exchange field does not exist and thus spin splitting cannot occur. The graphs of pumped currents have oscillatory behavior that the negative and positive values of currents show electrons flow in systems from left to right and right to left, respectively. Interestingly, the high pumped current (more than 50 μA for spin-up and spin-down currents or 100 μA for charge current) is a beneficial aspect for phosphorene-based nanodevices proposed in the present paper. Note that the charge current graph is the same as the
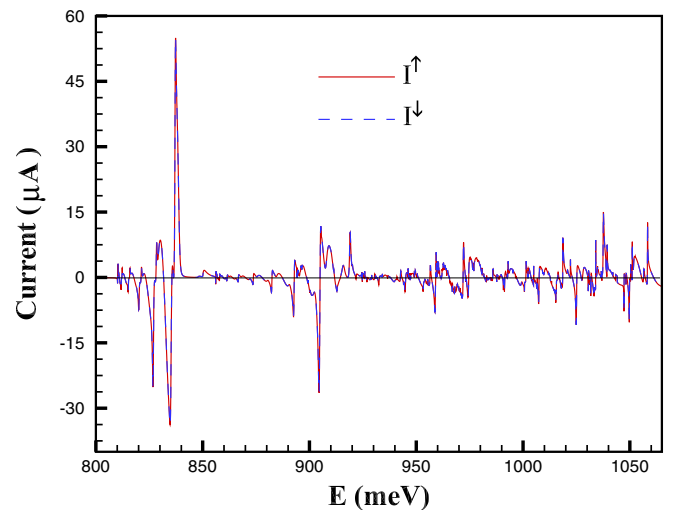

FIG. 3. Pumped spin-resolved currents $I^\uparrow$ and $I^\downarrow$ versus the Fermi energy E in the absence of exchange fields.
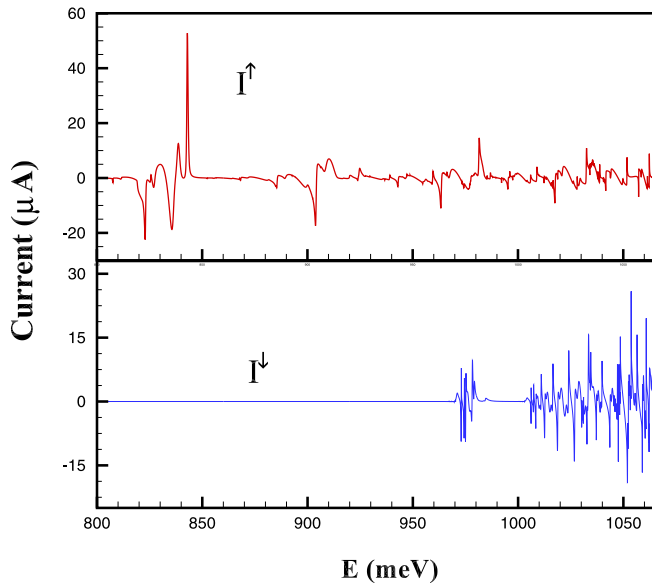
FIG. 4. Pumped spin-resolved currents $I^\uparrow$ and $I^\downarrow$ versus the Fermi energy in the presence of exchange fields with parallel configuration and normalized strength $M = 200$ meV. Upper (lower) panel shows spin-up (spin-down) current.

spin-up- and spin-down-current graphs but its value is the sum of spin-up and spin-down currents [see Eq. (15)].

In Fig. 4, we plot the pumped spin-up and spin-down currents in the presence of exchange fields with parallel configuration and normalized strength $M = 200$ meV. As shown in this figure, the exchange fields break the spin degeneracy and cause the pumped current to be spin polarized. For energy interval $800 < E < 970$ meV, spin-down current is zero and we have only the spin-up current. This is because the exchange fields raise the spin-down energy band and, as a consequence, this interval of energy is forbidden for electrons with spin down. So, as a result, this system acts as a spin-up filter device. The spin-up filter is perfect because the spin-down current is zero. Also, it can work in a wide interval of electron Fermi energy. It is worth noting that the Fermi energy can be tuned by changing the top gate voltage [45]. Increasing the exchange field, one can obtain spin-filtering current in a greater interval of electron energy. Furthermore, by reversing the direction of exchange fields, one can have a polarized current with spin down and the system can work as a perfect spin-down filter.

Figure 5 shows the spin current, charge current, and spin polarization in a small interval of Fermi energy (i.e., 1016–1028 meV). Here we consider exchange fields with parallel configuration and normalized strength $M = 200$ meV—same as Fig. 4. As shown in Fig. 5(a), the points indicated by A (B) show the values of Fermi energy at which spin-up (spin-down) current is zero and, according to Eq. (14), fully spin-polarized current could be obtained because at these points the spin polarization P_s is equal to ± 1 [see Fig. 5(b)]. In this case, the proposed device could work as a spin-up filter for $P_s = +1$ and spin-down filter for $P_s = -1$. The points indicated by black represent the values of energy at which both spin-up and spin-down currents are equal, so unpolarized current exists in these points. The spin polarization as a function of the
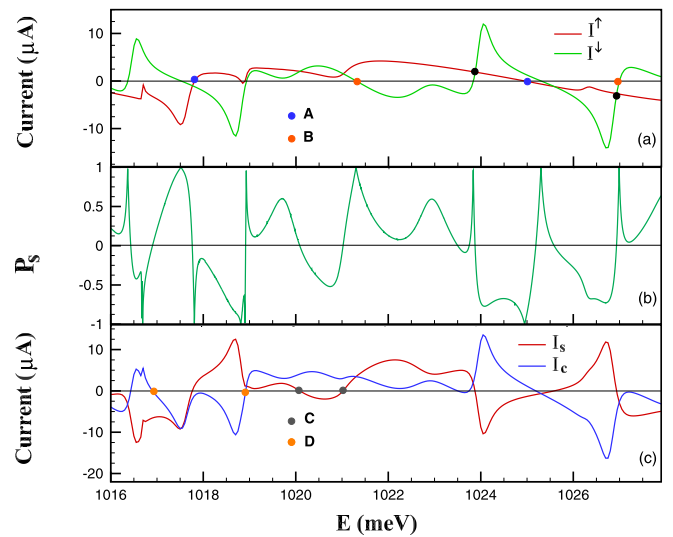

FIG. 5. (a) Pumped spin-resolved currents $I^\uparrow$ and $I^\downarrow$, (b) spin polarization P_s, and (c) pumped charge and spin currents versus the Fermi energy.

Fermi energy is shown in Fig. 5(b). It is observed that spin polarization P_s changes between -1 to $+1$ by variation of Fermi energy and one could adjust the spin polarization of pumped current at a desired value between -1 to $+1$ [37]. Spin and charge currents (I_s and I_c) are depicted in Fig. 5(c). The points indicated by C represent the values of Fermi energy at which spin current is zero, hence the pumped current is unpolarized. At points indicated by D, the charge current is zero and, according to Eq. (15), spin-up and spin-down currents are equal with opposite directions. Hence, at these points, we have pure spin current. As an interesting result, the proposed pumping device not only works as a spin filter but also works as a pure spin device.

The pumped spin current versus the Fermi energy is shown in Fig. 6 for parallel and antiparallel configurations
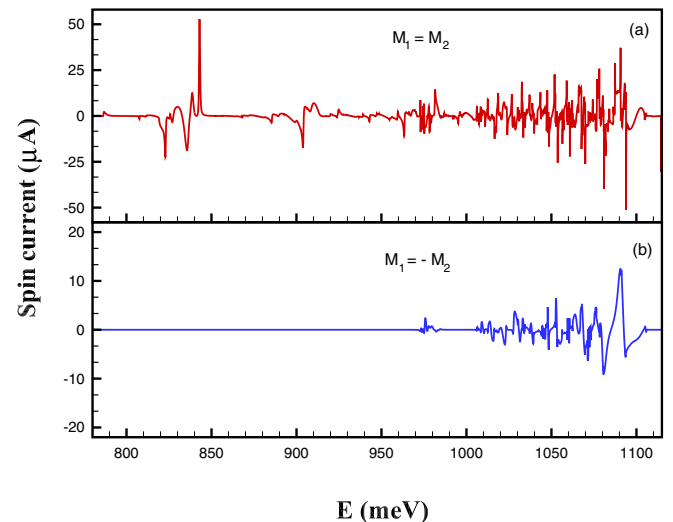

FIG. 6. Pumped spin current I_s versus the Fermi energy in the presence of exchange fields with (a) parallel and (b) antiparallel configurations.
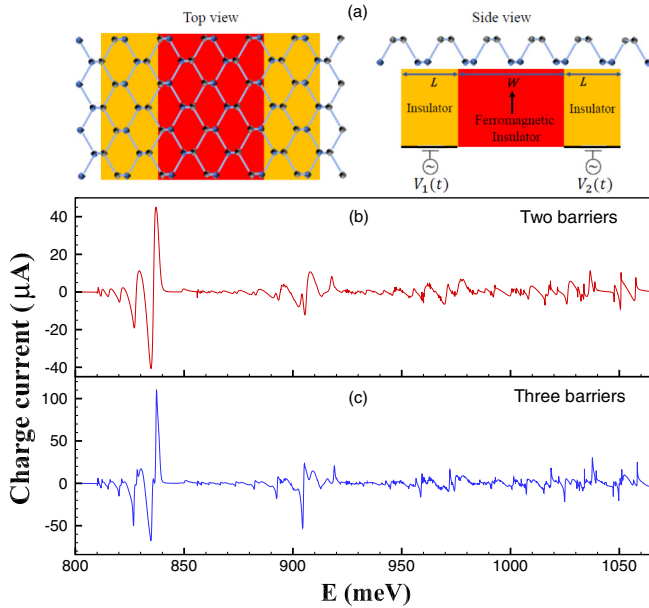
FIG. 7. (a) Top and side schematic views of a device with two oscillating potentials. Pumped charge current I_c in the absence of exchange fields versus the Fermi energy for a pumping device with (b) two and (c) three oscillating potentials.

FIG. 8. Pumped spin current versus the Fermi energy in the presence of uniaxial tensile strain with different values of ε_y applied on armchair direction (y direction, see Fig. 1). Here the static part of the potentials is chosen as $eV_{01} = eV_{02} = eV_{03} = 2300$ meV.

of exchange magnetic fields. It is observed that if the exchange magnetic fields are parallel, as shown in Fig. 1, the spin-pumped current has nonzero values for $E < 970$ meV, which is due to the spin-up current as shown in Fig. 4. Note that in this configuration, spin-down current is zero for $E < 970$ meV [see Fig. 4(b)]. For the case of antiparallel configuration, the spin current (also spin-up and spin-down currents) is zero in this range of energy ($E < 970$ meV). This is because if we suppose that an electron with spin up is injected to the system from the left side and the first (second) exchange field has an antiparallel (parallel) magnetization related to the electron spin direction, the first exchange field acts as a barrier for this electron, as shown in Fig. 2. Also, in this configuration, if an electron with spin down is injected into the system, the second exchange field acts as a barrier for this electron. Hence, for an electron with each type of spin direction, one of the exchange fields raises the electron energy band and causes placement of this range of energy in the band-gap interval. As we can see in Fig. 6(b), for $E > 970$ meV there is a nonzero current for antiparallel configuration because this range of energy does not place in the band-gap interval.

In this paper, we propose a pumping device with three oscillating potentials. Now we compare the pumped current of this device with a conventional two oscillating potential device [36,44] and the results at the same conditions are shown in Fig. 7. A schematic view of a pumping device with two oscillating potentials is shown in Fig. 7(a). As shown in Figs. 7(b) and 7(c), the pumped current for three potentials is about two times greater than that of two potentials. Thus, by increasing the number of potentials (from two to three), one could significantly enhance the pumped currents. We know that the phase difference between oscillating potentials and thereby unequal scattering of carriers cause generation of a
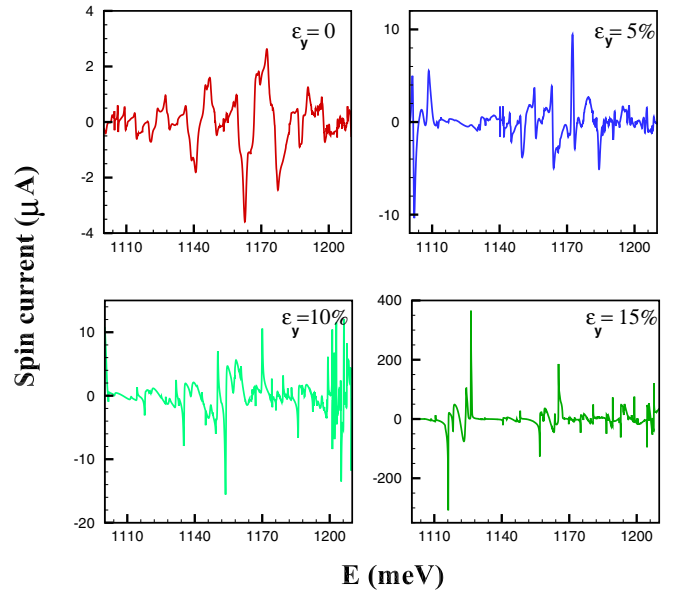
pumped current. So, in the case of three potential barriers, charge carriers spend a longer time in the barrier regions, which causes the scattering time to be longer and, as a result, the pumped current increases. The pumped current for a two-barrier device can be obtained in the limiting case of a three-barrier one, when the length of right barrier and right ferromagnetic region of three-barrier device go to zero (see Appendix B).

Although there are many studies in the literature related to the effects of strain on transport properties in 2D materials (see e.g., Refs. [21,46–50]), there are only a few studies on the role of strain in quantum pumping in these materials [51–53]. We now study the effects of strain on quantum pumping in phosphorene and the results are shown in Fig. 8. This figure shows the effects of uniaxial tensile strain on pumped spin current for different values of ε_y ($\varepsilon_y = 0.05, 0.1,$ and 0.15). Here, the graph of the unstrained system ($\varepsilon_y = 0$) is shown in the figure for comparison. As we can see in this figure, the pumped current significantly enhances by applying the strain. For instance, for strain with $\varepsilon_y = 0.15$, the maximum pumped current increases by two orders of magnitude relative to the unstrained system, which shows high sensitivity of pumped current to strain. As another result, the proposed device based on phosphorene could also be used for straintronic devices such as strain sensors and strain switches. The pumped current enhancement, in the presence of strain, is due to the density of states increment in the phosphorene channel and hence the increment of accessible states for carriers [54].

Now, for showing the prominence of phosphorene-based pumping devices other than common 2D materials, we compare the pumped charge current of phosphorene with graphene and silicene. In Fig. 9, the pumped charge current versus the Fermi energy is plotted for graphene, silicene, and phosphorene in the presence of three potential barriers. The
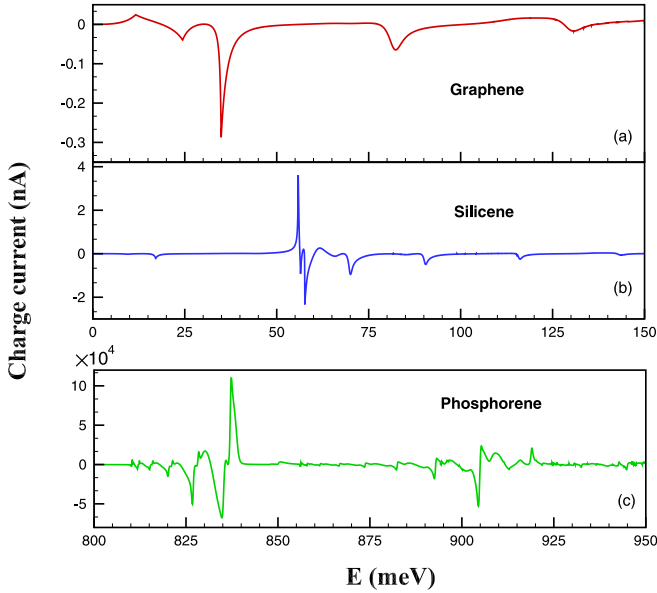
FIG. 9. Pumped charge current in the absence of exchange fields versus the Fermi energy for (a) graphene, (b) silicene, and (c) phosphorene-based pumping devices with three oscillating potentials.

calculations are made for the same conditions except, due to the large (1.4 eV) energy gap of phosphorene, the range of energy in Fig. 9(c) is selected greater than Figs. 9(a) and 9(b). It is seen that the maximum value of charge current magnitude in phosphorene is four and five orders of magnitude greater than those of silicene and graphene. This is because of an intrinsic anisotropic behavior of phosphorene due to its puckered structure and its long phase-coherent that is, effective in transport properties [55]. Furthermore, the pumped charge current in the phosphorene-based device is two orders of magnitude greater than the current in MoS$_2$-based device that has been studied recently [37]. This is because of the higher mobility and less effective mass of carrier in phosphorene than MoS$_2$ [10,37]. From the technological point, the measurement and manipulation of pumped charge and spin currents with microampere order in phosphorene [56] are simpler than nanoampere currents in graphene [44]. So these results present the advantages of phosphorene-based devices versus graphene-based ones and introduce this material as a good candidate in spintronics and straintronic applications [9,10].

IV. SUMMARY AND CONCLUSION

In this paper, we have studied the spin- and charge-pumping properties in a monolayer phosphorene using S-matrix approach. Here we have proposed a pumping device with three external ac gate voltages as oscillating potential barriers that are responsible for generating the dc pumped current. In the presence of exchange field induced by proximity effect of ferromagnetic insulators, we have determined the conditions in which fully spin-polarized current and pure spin current can be obtained. It has been shown that three-barrier pumping devices have some advantages relative to two-barrier ones such as higher pumped currents. We have also studied

the effect of strain on pumped currents and shown that the strain causes an increase of the pumped currents by up to two orders of magnitude. As a result, the proposed device could be used as strain sensors and strain switches, which are two important devices in straintronics. A comparison between the pumped current in phosphorene and some other 2D materials shows that the pumped current in phosphorene is two, four, and five orders of magnitude greater than the pumped current in MoS$_2$, silicene, and graphene, respectively, which is due to the anisotropic behavior and the high carrier mobility of phosphorene. The results of this paper could motivate researchers to consider phosphorene as a promising candidate for fabricating spintronic and straintronic devices with low power consumption and large processing speeds.

APPENDIX A

Here we explain the method for changing the integral variable in Eq. (13) from k_x to ϕ. Using Eq. (2), the eigenvalues of the Hamiltonian $\hat{H}_0$ are given by

$$E_0 = u_0 + \eta_x k_x^2 + \eta_y k_y^2 \pm \sqrt{\left(\delta + \gamma_x k_x^2 + \gamma_y k_y^2\right)^2 + (\chi k_y)^2}. \tag{A1}$$

Substituting $k_x = -k\sin\phi$ and $k_y = k\cos\phi$ and solving the above equation, we have

$$k = \sqrt{\frac{-b \pm \sqrt{b^2 - 4ac}}{2a}}, \tag{A2}$$

where

$$
\begin{aligned}
a &= (\eta_x \sin^2\phi + \eta_y \cos^2\phi)^2 - (\gamma_x \sin^2\phi + \gamma_y \cos^2\phi)^2, \\
b &= -2(E_0 - u_0)(\eta_x \sin^2\phi + \eta_y \cos^2\phi) - (\chi \cos\phi)^2 \\
&\quad - 2\delta(\gamma_x \sin^2\phi + \gamma_y \cos^2\phi), \\
c &= (E_0 - u_0)^2 - \delta^2.
\end{aligned} \tag{A3}
$$

Since k depends on ϕ, derivation of k_x can be written as

$$dk_x = \left[-(\sin\phi)\frac{\partial k}{\partial \phi} - k(\cos\phi) \right] d\phi, \tag{A4}$$

where

$$\frac{\partial k}{\partial \phi} = \frac{\left[\left(-b' - \frac{2bb' - 4a'c}{2\sqrt{b^2 - 4ac}}\right) - 2a'k^2 \right]}{4ak}, \tag{A5}$$

and

$$
\begin{aligned}
a' &= \frac{\partial a}{\partial \phi} = 2(\sin 2\phi)[(\eta_x \sin^2\phi + \eta_y \cos^2\phi)(\eta_x - \eta_y) \\
&\quad - (\gamma_x \sin^2\phi + \gamma_y \cos^2\phi)(\gamma_x - \gamma_y)], \\
b' &= \frac{\partial b}{\partial \phi} = (\sin 2\phi)[-2(E_0 - u_0)(\eta_x - \eta_y) + \chi^2 \\
&\quad - 2\delta(\gamma_x - \gamma_y)].
\end{aligned} \tag{A6}
$$

APPENDIX B

The *S* matrix for the three-barrier system can be written as

$$S = [(r, t)^T (t', r')^T],$$ (B1)

where the reflection and transmission coefficients for incident electrons from left side of system are, respectively, given by [42]

$$r = \left(r_b + \frac{t_b' r_4 t_b}{1 - r_b' r_4}\right) + \frac{\left(\frac{t_b' t_4'}{1 - r_b' r_4}\right) r_5 \left(\frac{t_b t_4}{1 - r_b' r_4}\right)}{1 - \left(r_4' + \frac{t_4 r_b' t_4'}{1 - r_b' r_4}\right) r_5}$$ (B2)

and

$$t = \frac{\left(\frac{t_b t_4}{1 - r_b' r_4}\right) t_5}{1 - \left(r_4' + \frac{t_4 r_b' t_4'}{1 - r_b' r_4}\right) r_5},$$ (B3)

and the reflection and transmission coefficients for incident electrons from the right side can be written as

$$r' = r_5' + \frac{t_5 \left(r_4' + \frac{t_4 r_b' t_4'}{1 - r_b' r_4}\right) t_5'}{1 - \left(r_4' + \frac{t_4 r_b' t_4'}{1 - r_b' r_4}\right) r_5}$$ (B4)

and

$$t' = \frac{\left(\frac{t_b' t_4'}{1 - r_b' r_4}\right) t_5'}{1 - \left(r_4' + \frac{t_4 r_b' t_4'}{1 - r_b' r_4}\right) r_5},$$ (B5)

respectively. In Eqs. (B2)–(B5),

$$r_b = \left(r_1 + \frac{t_1' r_2 t_1}{1 - r_1' r_2}\right) + \frac{\left(\frac{t_1' t_2'}{1 - r_1' r_2}\right) r_3 \left(\frac{t_1 t_2}{1 - r_1' r_2}\right)}{1 - \left(r_2' + \frac{t_2 r_1' t_2'}{1 - r_1' r_2}\right) r_3},$$ (B6)

$$t_b = \frac{\left(\frac{t_1 t_2}{1 - r_1' r_2}\right) t_3}{1 - \left(r_2' + \frac{t_2 r_1' t_2'}{1 - r_1' r_2}\right) r_3},$$ (B7)

$$r_b' = r_3' + \frac{t_3 \left(r_2' + \frac{t_2 r_1' t_2'}{1 - r_1' r_2}\right) t_3'}{1 - \left(r_2' + \frac{t_2 r_1' t_2'}{1 - r_1' r_2}\right) r_3},$$ (B8)

$$t_b' = \frac{t_3' \left(\frac{t_1' t_2'}{1 - r_1' r_2}\right)}{1 - \left(r_2' + \frac{t_2 r_1' t_2'}{1 - r_1' r_2}\right) r_3},$$ (B9)

where r_j and t_j ($j = 1, 2, ..., 5$) are the reflection and transmission coefficients for incident electrons from the left side of region j and r_j' and t_j' are the reflection and transmission coefficients for incident electrons from the right side of region j. Note that in Eqs. (B2)–(B9), for convenience in writing, we have used $j = 1, 2, ..., 5$ to show the number of regions of the system instead of $j = $ I, II,..., V (see Fig. 1). In the limiting case, when the length of right potential barrier, L, and right ferromagnetic well, W, go to zero, the three-barrier pumping device becomes a two-barrier one. In this case, $r_4 = r_4' = r_5 = r_5'$ go to zero, and $t_4 = t_4' = t_5 = t_5'$ go to 1 and Eqs. (B2)–(B5) reduce to Eqs. (B6)–(B9), which show the reflection and transmission coefficients for the two-barrier system. Now, the *S* matrix for the two-barrier system can be written as $S_{(2b)} = [(r_b, t_b)^T (t_b', r_b')^T]$ and the pumped current for this system is given by substituting $S_{(2b)}$ into Eq. (12) and using Eq. (13).

[1] H. Dery, H. Wu, B. Ciftcioglu, M. Huang, Y. Song, R. Kawakami, J. Shi, I. Krivorotov, I. Zutic, and L. J. Sham, IEEE Trans. Electron Devices **59**, 259 (2011).

[2] N. Takagi, C.-L. Lin, K. Kawahara, E. Minamitani, N. Tsukahara, M. Kawai, and R. Arafune, Prog. Surf. Sci. **90**, 1 (2015).

[3] A. Splendiani, L. Sun, Y. Zhang, T. Li, J. Kim, C.-Y. Chim, G. Galli, and F. Wang, Nano Lett. **10**, 1271 (2010).

[4] H. Huang, B. Jiang, X. Zou, X. Zhao, and L. Liao, Sci. Bull. **64**, 1067 (2019).

[5] H. Liu, A. T. Neal, Z. Zhu, Z. Luo, X. Xu, D. Tomanek, and P. D. Ye, ACS Nano **8**, 4033 (2014).

[6] S. P. Koenig, R. A. Doganov, H. Schmidt, A. H. Castro Neto, and B. Ozyilmaz, Appl. Phys. Lett. **104**, 103106 (2014).

[7] M. Buscema, D. J. Groenendijk, S. I. Blanter, G. A. Steele, H. S. J. van der Zant, and A. Castellanos-Gomez, Nano Lett. **14**, 3347 (2014).

[8] F. Xia, H. Wang, and Y. Jia, Nat. Commun. **5**, 4458 (2014).

[9] L. Kou, C. Chen, and S. C. Smith, J. Phys. Chem. Lett. **6**, 2794 (2015).

[10] A. Carvalho, M. Wang, X. Zhu, A. S. Rodin, H. Su, and A. H. Castro Neto, Nat. Rev. Mater. **1**, 16061 (2016).

[11] S. P. Dash, S. Sharma, R. S. Patel, M. P. de Jong, and R. Jansen, Nature **462**, 491 (2009).

[12] L. Li, Y. Yu, G. J. Ye, Q. Ge, X. Ou, H. Wu, D. Feng, X. H. Chen, and Y. Zhang, Nat. Nanotechnol. **9**, 372 (2014).

[13] W. Lu, H. Nan, J. Hong, Y. Chen, C. Zhu, Z. Liang, X. Ma, Z. Ni, C. Jin, and Z. Zhang, Nano Res. **7**, 853 (2014).

[14] R. Fei and L. Yang, Nano Lett. **14**, 2884 (2014).

[15] X. Wang, A. M. Jones, K. L. Seyler, V. Tran, Y. Jia, H. Zhao, H. Wang, L. Yang, X. Xu, and F. Xia, Nat. Nanotechnol. **10**, 517 (2015).

[16] M. Elahi, K. Khaliji, S. M. Tabatabaei, M. Pourfath, and R. Asgari, Phys. Rev. B **91**, 115412 (2015).

[17] W.-J. Zhu, W. Zhao, and J.-W. Ding, J. Phys.: Condens. Matter **30**, 33LT01 (2018).

[18] B. Zhou, B. Zhou, X. Zhou, and G. Zhou, J. Phys. D: Appl. Phys. **50**, 045106 (2016).

[19] A. Chaudhury, S. Majumder, and S. J. Ray, Phys. Rev. Appl. **11**, 024056 (2019).

[20] D. Cakir, H. Sahin, and F. M. Peeters, Phys. Rev. B **90**, 205421 (2014).

[21] A. S. Rodin, A. Carvalho, and A. H. Castro Neto, Phys. Rev. Lett. **112**, 176801 (2014).

[22] H. Hedayati Kh and E. Faizabadi, J. Phys.: Condens. Matter **30**, 085303 (2018).

[23] M. A. M. Keshtan and M. Esmaeilzadeh, J. Phys. D: Appl. Phys. **48**, 485301 (2015).

[24] A. Avsar, J. Y. Tan, M. Kurpas, M. Gmitra, K. Watanabe, T. Taniguchi, J. Fabian, and B. Ozyilmaz, Nat. Phys. **13**, 888 (2017).

[25] C. G. Rocha, Luis E. F. Foa Torres, and G. Cuniberti, Phys. Rev. B **81**, 115435 (2010).

[26] D. J. Thouless, Phys. Rev. B **27**, 6083 (1983).

[27] M. Switkes, C. M. Marcus, K. Campmana, and A. C. Gossard, Science **283**, 1905 (1999).

[28] I. L. Aleiner and A. V. Andreev, Phys. Rev. Lett. **81**, 1286 (1998).

[29] M. Moskalets and M. Buttiker, Phys. Rev. B **66**, 205320 (2002); **72**, 035324 (2005).

[30] M. Moskalets and M. Buttiker, Phys. Rev. B **75**, 035315 (2007).

[31] L. E. F. Foa Torres, Phys. Rev. B **72**, 245339 (2005).

[32] M. D. Blumenthal, B. Kaestner, L. Li, S. Giblin, T. J. B. M. Janssen, M. Pepper, D. Anderson, G. Jones, and D. A. Ritchie, Nat. Phys. **3**, 343 (2007).

[33] S. Souma and M. Ogawa, Appl. Phys. Lett. **104**, 183103 (2014).

[34] R. P. Tiwari and M. Blaauboer, Appl. Phys. Lett. **97**, 243112 (2010).

[35] L. H. Ingaramo and L. E. F. Foa Torres, Appl. Phys. Lett. **103**, 123508 (2013).

[36] H. Khani, M. Esmaeilzadeh, and F. Kanjouri, Nanotechnology **27**, 495202 (2016).

[37] H. Khani, M. Esmaeilzadeh, and F. Kanjouri, Phys. Chem. Chem. Phys. **19**, 14170 (2017).

[38] J. M. Pereira, Jr. and M. I. Katsnelson, Phys. Rev. B **92**, 075437 (2015).

[39] E. Taghizadeh Sisakht, F. Fazileh, M. H. Zare, M. Zarenia, and F. M. Peeters, Phys. Rev. B **94**, 085417 (2016).

[40] H. Duan, M. Yang, and R. Wang, Physica E **81**, 177 (2016).

[41] A. N. Rudenko and M. I. Katsnelson, Phys. Rev. B **89**, 201408(R) (2014).

[42] S. Datta, *Electronic Transport in Mesoscopic Systems* (Cambridge University Press, Cambridge, 1995).

[43] P. W. Brouwer, Phys. Rev. B **58**, R10135(R) (1998).

[44] Q. Zhang, K. S. Chan, and Z. Lin, Appl. Phys. Lett. **98**, 032106 (2011).

[45] E. Prada, P. San-Jose, and H. Schomerus, Phys. Rev. B **80**, 245414 (2009).

[46] M. Farokhnezhad, M. Esmaeilzadeh, and Kh. Shakouri, Phys. Rev. B **96**, 205416 (2017).

[47] V. M. Pereira, A. H. Castro Neto, and N. M. R. Peres, Phys. Rev. B **80**, 045401 (2009).

[48] R. C. Xiao, D. F. Shao, W. J. Lu, H. Y. Lv, J. Y. Li, and Y. P. Sun, Appl. Phys. Lett. **109**, 122604 (2016).

[49] V. Shukla, A. Grigoriev, N. K. Jena, and R. Ahuja, Phys. Chem. Chem. Phys. **20**, 22952 (2018).

[50] S. J. Ray and M. V. Kamalakar, Phys. Chem. Chem. Phys. **20**, 13508 (2018).

[51] Y. Jiang, T. Low, K. Chang, M. I. Katsnelson, and F. Guinea, Phys. Rev. Lett. **110**, 046601 (2013).

[52] T. Low, Y. Jiang, M. Katsnelson, and F. Guinea, Nano Lett. **12**, 850 (2012).

[53] F. Kanjouri, S. P. Pishekloo, and H. Khani, J. Phys.: Condens. Matter **31**, 305304 (2019).

[54] N. D. Hien, M. Davoudiniya, K. Mirabbaszadeh, L. T. T. Phuong, and M. Yarmohammadi, Chem. Phys. **522**, 249 (2019).

[55] F. Wu, D. Rocca, and Y. Ping, J. Mater. Chem. C **7**, 12891 (2019).

[56] S. Das, W. Zhang, M. Demarteau, A. Hoffmann, M. Dubey, and A. Roelofs, Nano Lett. **14**, 5733 (2014).